

Quantitative Power Flow Characterization of Energy Harvesting Shock Absorbers by Considering Motion Bifurcation

Jing Li ^{1,*} , Peiben Wang ¹, Yuewen Gao ², Dong Guan ¹  and Shengquan Li ³ 

¹ Collage of Mechanical Engineering, Yangzhou University, Yangzhou 225127, China

² Collage of Civil Engineering, Yangzhou Polytechnic Institute, Yangzhou 225127, China

³ Collage of Electrical, Energy and Power Engineering, Yangzhou University, Yangzhou 225127, China

* Correspondence: yzlijing@yzu.edu.cn

Abstract: Vibration energy harvesting technology can capture ambient energy forms. Using an energy harvesting shock absorber (EHSA) is one of the methods to achieve this function. The EHSA with mechanical motion rectifier (MMR) has motion bifurcation, which can improve energy harvesting performance and reduce the impact between gears. However, the motion bifurcation makes it difficult to quantitatively predict the vibrational energy dissipation and energy harvesting of the MMR–EHSA. Evaluating the performance of an MMR–EHSA during the design phase becomes highly complex. In this paper, a novel nonlinear dynamics model of MMR–EHSAs is established to solve motion bifurcation and quantitative power flow. Furthermore, the proposed MMR–EHSA prototype is fabricated, and dynamics testing is initiated to verify the theoretical model under harmonic vibration. The testing results show that the theoretical model can predict the working characterization of MMR–EHSAs. The resistance of optimal harvesting energy and maximum damping power is revealed by the quantitative power flow model under harmonic vibration. In addition, the working performance under random vibration is discussed. The proposed nonlinear dynamics model has advantages when solving random vibration input and has potential for practical application.



Citation: Li, J.; Wang, P.; Gao, Y.; Guan, D.; Li, S. Quantitative Power Flow Characterization of Energy Harvesting Shock Absorbers by Considering Motion Bifurcation. *Energies* **2022**, *15*, 6887. <https://doi.org/10.3390/en15196887>

Academic Editor:
Abdessattar Abdelkefi

Received: 23 July 2022
Accepted: 16 September 2022
Published: 20 September 2022

Publisher's Note: MDPI stays neutral with regard to jurisdictional claims in published maps and institutional affiliations.



Copyright: © 2022 by the authors. Licensee MDPI, Basel, Switzerland. This article is an open access article distributed under the terms and conditions of the Creative Commons Attribution (CC BY) license (<https://creativecommons.org/licenses/by/4.0/>).

Keywords: power flow; motion bifurcation; energy harvesting; nonlinear dynamics

1. Introduction

In recent years, a plethora of research initiatives have been carried out in the field of energy harvesting [1–4]. There are three main types of energy harvesting: piezoelectric [5,6], nano-electrostatic [7,8], and mechanical electromagnetic [9–12]. The mechanical electromagnetic method is one of the most popular methods due to its wide range of applications [13]. The mechanical electromagnetic method is also referred to as an energy harvesting shock absorber (EHSA) [14]. EHSAs have two types. These are often classified as linear and rotational EHSAs, also referred to as direct-drive [1,15,16] and indirect-drive EHSA models [17]. In linear EHSAs, the linear movement is utilized to turn the mechanical energy into electric energy. Rotational EHSAs translate the oscillatory movement into bidirectional rotation. Generally, conventional EHSA methods, such as rack-pinion [18] and ball-screw [19] models, demonstrate this conversion of oscillatory vibration into bidirectional rotation. However, the other model, i.e., the mechanical motion rectifier (MMR) [20], initiates the change of bidirectional vibration into unidirectional rotation.

In 2013, Li et al. [21] designed a vehicular rack-pinion EHSA. The EHSA can realize asymmetric damping characteristics by changing the load resistance value in different strokes. The road test showed that the EHSA could reflect the roughness of the road using the voltage the EHSA generated. However, EHSA parts will produce a vibrational impact when the vibration direction changes. Therefore, Li et al. [20] proposed an EHSA with an MMR. The experiment and simulation results have shown that MMRs can reduce the impact between parts and enhance energy harvesting. Since then, MMR–EHSAs has attracted extensive attention among researchers.

The MMR is a mechanism that converts oscillating linear motion into unidirectional rotational motion by utilizing two roller clutches. The rolling clutch can only transmit unidirectional torque. The MMR has a kind of motion bifurcation. The motion bifurcation embodies the roller clutch motion with no change in direction; however, torque transmission is interrupted. Before the moment of motion bifurcation, the MMR's motion state is called the engagement state. After the moment, it is called a disengagement state. This motion bifurcation reduces the impact between MMR–EHSAs parts and increases the harvested energy [22].

The dynamic characteristics of MMR–EHSAs in the engagement state and disengagement state are different. An EHSAs without an MMR is the basis of studying MMR–EHSAs. The MMR–EHSAs engagement state has the same dynamics and power flow characteristics as an EHSAs without an MMR. Xie et al. [23,24] designed a multi-generator EHSAs without an MMR. The power flow of the multi-generator was studied. The damping force was changed by controlling the number of working generators. Unlike changing the damping force by adjusting the load resistance, the waste of harvesting electric energy can be reduced by changing the number of operating generators. Zhu et al. [25] designed an EHSAs without an MMR. He developed a quantitative power flow model for EHSAs and predicted the vibrational energy dissipation performance and energy harvesting performance of an EHSAs without an MMR. The dynamics model treated friction as the sum of Coulomb friction and viscous friction. The theoretical model can predict the EHSAs's force–displacement curve and harvesting power. The method of considering friction force provides a reference for researchers. Zuo et al. [26] proposed an analytical method to solve the bifurcation threshold of MMR–EHSAs. The analytical method can accurately predict working characteristics and has been widely cited by many researchers for exploring the characteristics of MMR–EHSAs under harmonic excitation. Zuo et al. designed an MMR–EHSAs that could be used in water [27] and land transportation [28], biology [29], and other fields. The MMR–EHSAs demonstrated good energy harvesting performance through testing on both the ocean and on highways. However, the working characteristics of MMR–EHSAs under random vibration have rarely been studied through the analytical method. Because motion bifurcation is highly unpredictable under random vibration, it is challenging to obtain the analytical solution to the motion bifurcation threshold under random vibration. Yang et al. [30] designed a bicycle cushion MMR–EHSAs. The nonlinear dynamics model and output power model were established. Although the theoretical model contained motion bifurcations, the simulation results for damping force did not show motion bifurcation transmission characteristics. This also reflected the requirement of studying the motion bifurcation characteristics. Zhang et al. designed an MMR–EHSAs with different transmission structures, such as double ball screw drives [31], tree-like drives [32], and ball screw drives with different rotations [33]. The effects of different transmission structures on the MMR–EHSAs's working efficiency were compared, and the results provided criteria for the design of MMR–EHSAs.

Researchers have greatly expanded the application of EHSAs. The damping performance and energy harvesting performance of EHSAs have been studied extensively. The accuracy of friction predictions has also been improved. Previous studies have found that the theoretical research into MMR–EHSAs with random vibration input is insufficient. The uncertainty of motion bifurcation makes it difficult to evaluate vibrational dissipation and energy harvesting, especially with random vibration input. Therefore, a new, dynamic MMR–EHSAs theory suitable for studying random vibration is required for further research deliberations, which could help provide a theoretical basis for designing MMR–EHSAs. The contributions are listed as follows:

- (1) A novel numerical iterative method was proposed that fills in the blanks from the theoretical solution for MMR–EHSAs with random vibration input. Based on the proposed theoretical model, the power flow of MMR–EHSAs in different working states is established. Through the power flow model, the working effect of MMR–EHSAs

can be effectively evaluated in the preliminary stages, which helps the design and application of MMR–EHSA.

- (2) The working characteristics of MMR–EHSA are demonstrated by studying common harmonic excitation. The optimal damping force resistance is revealed. The power flow model can obtain the optimal energy harvesting resistance.

This paper is organized as follows. Section 2 introduces the working principle and motion bifurcation of MMR–EHSA. In Section 3, the nonlinear dynamics model for MMR–EHSA established, the numerical iterative bifurcation model and analytical bifurcation model are presented, and a quantitative power flow model is established. In Section 4, dynamics testing is conducted to verify the proposed model under harmonic vibration. Section 5 discusses the vibrational energy dissipation and energy harvesting processes under harmonic and random vibration. Finally, the conclusions are presented in Section 6.

2. Design and Working Principle

An EHSA is a combination of inertia and an electromagnetic damper [25]. An MMR can reduce the impact of inertia from the parts when the external excitation is in the deceleration and reversing stage. As shown in Figure 1, the MMR–EHSA is designed based on a rack and pinion transmission structure. It consists of three modules: an MMR, a transmission module, and a generator module. The MMR can convert the oscillatory vibration of the rack into the one-way rotation motion of the shaft through two roller clutch bearings. The transmission module increases the velocity of the generator and amplifies the damping force generated by the generator. In this process, the EHSA dissipates input vibrational energy and harvests part of the dissipated vibrational energy into electrical energy. The generator module can harvest electrical energy using the excitation input. Simultaneously, different resistances connected to the positive and negative poles of the generator can produce different electromagnetic damping forces and change the damping performance and energy harvesting performance of the MMR–EHSA. Table 1 lists parameters related to the MMR–EHSA.

The MMR–EHSA has two kinds of working states: engagement and disengagement. The damping force of the MMR–EHSA will produce small and continuous change in the engagement state, before then causing a sudden change in the path of the transmission. This sudden change is the motion bifurcation of the MMR–EHSA. Figure 2 reveals the process of motion bifurcation under harmonic excitation. The specific process of motion bifurcation in a half cycle can be divided into four stages according to the relationships of velocities among gear 1, gear 2, and their coupling. Stage 1 is the engagement state, where gear 1 with high velocity keeps roller clutch 1 engaged and drives the coupling. The velocity of gear 1 then decreases, making the MMR enter state 2, which is the disengagement state. The velocity of the coupling is higher than the velocity of gear 1. The demarcation between state 1 and state 2 is the motion bifurcation threshold. In the demarcation moment, the work stage of roller clutch 1 changes from engagement to disengagement. As the rack moves from the upward stroke to the downward stroke, the MMR enters state 3. The velocity of gear 2 is higher than the velocity of gear 1. The demarcation between state 2 and state 3 is the top dead center of the MMR–EHSA. The velocity of gear 1 and gear 2 is zero, but the coupling keeps rotating. When the velocity of gear 2 reaches the coupling velocity, roller clutch 2 from the disengagement state enters the engagement state. The MMR then enters state 4. Gear 2 will carry the coupling as it rotates in state 4. In addition, the downward stroke to upward stroke has a similar transmission process as the one explained above.

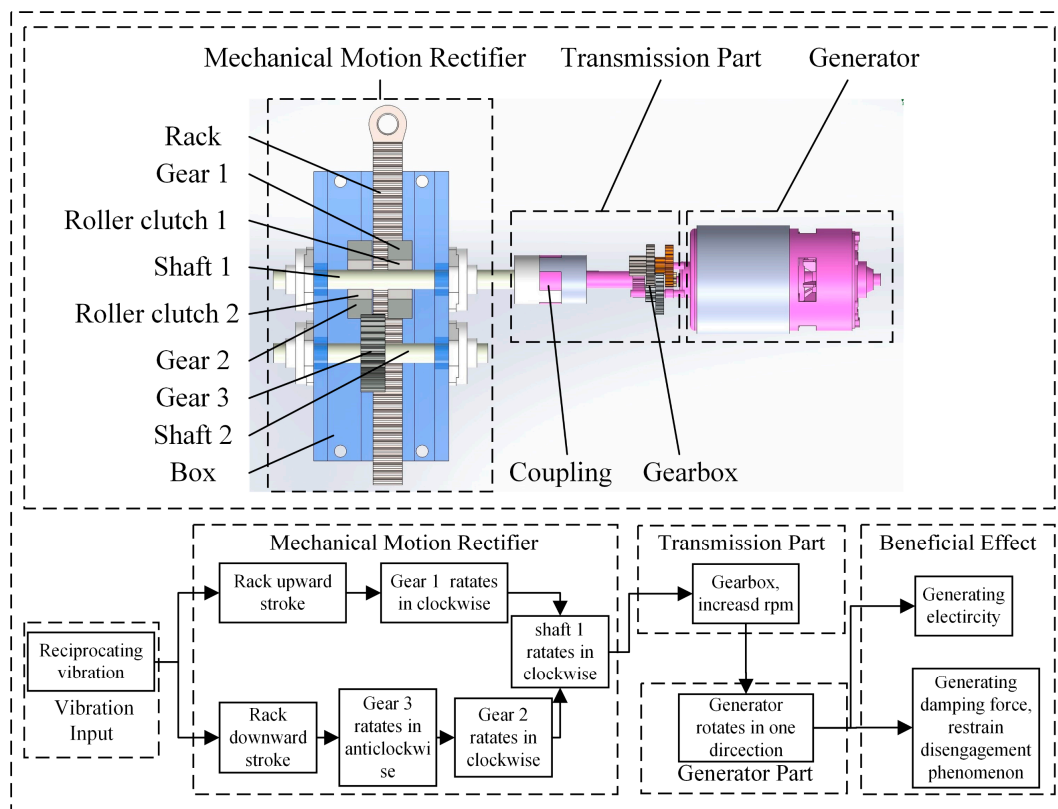


Figure 1. Structure of the MMR–EHSA.

Table 1. Specified parameters.

Symbol	Value	Physical Understanding
m_r	0.491 kg	inertia coefficient of the rack
J_{g1}	$7.066 \times 10^{-6} \text{ kg}\cdot\text{m}^2$	rotational inertia of gear 1
J_{g2}	$7.066 \times 10^{-6} \text{ kg}\cdot\text{m}^2$	rotational inertia of gear 2
J_{g3}	$7.066 \times 10^{-6} \text{ kg}\cdot\text{m}^2$	rotational inertia of gear 3
J_c	$8.106 \times 10^{-6} \text{ kg}\cdot\text{m}^2$	rotational inertia of the coupling
J_{gr}	$32.212 \times 10^{-6} \text{ kg}\cdot\text{m}^2$	rotational inertia of the generator
i_{gb}	0.045	transmission ratio of the gearbox
r_g	15 mm	gear radius
k_e	0.048 V/rad	back electromotive voltage constant
k_t	0.090 N·m/A	torque constant
R_{coil}	5.5 Ω	resistance of the generator coil
f_{s1}	1.7 N	slide friction force of the MMR
f_{s2}	17.06 N	slide friction force of the gearbox and generator
c_{b1}	7.5 N·s/m	equivalent mechanical damping coefficient of the MMR
c_{b2}	75.6 N·s/m	equivalent mechanical damping coefficient of the gearbox and generator
n_{00}	0.011 m^{-1}	cutoff frequency
u	16.67 m/s	horizontal movement velocity
$S_q(n_0)$	$64 \times 10^{-6} \text{ m}^3$	roughness index

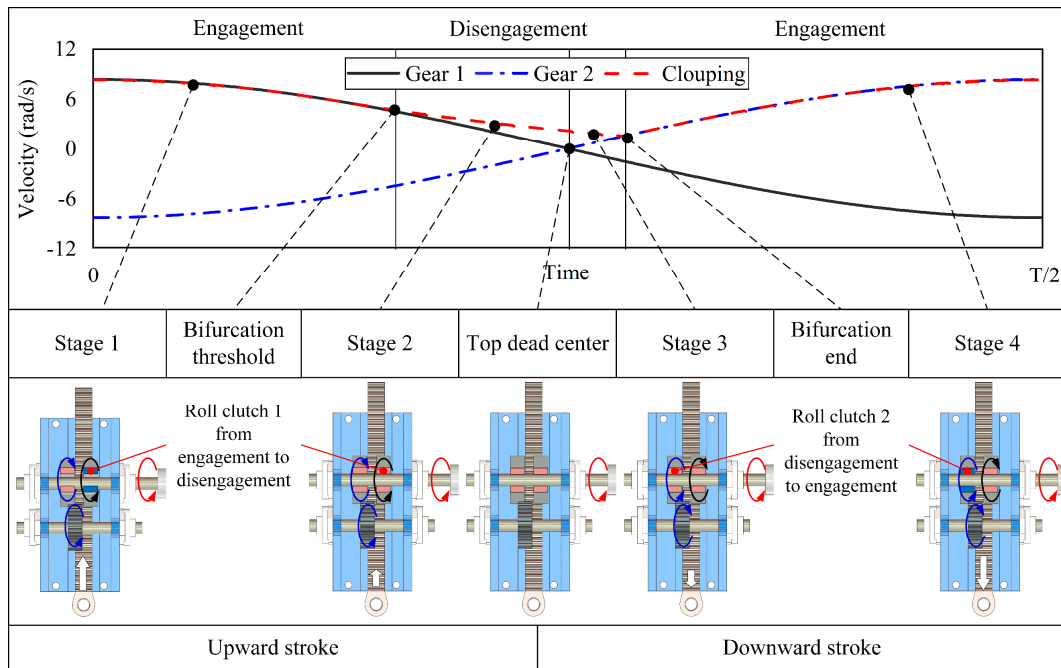


Figure 2. Process of motion bifurcation under harmonic excitation.

3. Nonlinear Dynamics Model of MMR–EHSAs

The proposed nonlinear dynamics model comprises two parts: the nonlinear total damping force model and the motion bifurcation model. The motion bifurcation model is used to determine the nonlinear state so as to complete the solution cooperatively. Analytical methods for solving MMR–EHSAs motion bifurcation are used by a fairly large number of researchers. A novel numerical iteration method is proposed in this paper. This method has advantages when solving complex excitation.

3.1. Nonlinear Total Damping Force Model of MMR–EHSAs

The composition of MMR–EHSAs damping force is different between the engagement behavior and the disengagement behavior. The total damping force is generated by the MMR, the gearbox, and the generator in engagement behaviors. In disengagement behaviors, the total damping force is generated by the MMR. The other parts cannot transmit damping force through the disengagement roller clutch. In this paper, the force generated by the EHSAs is regarded as having three parts: inertia force, electromagnetic damping force, and dissipation damping force. As shown in Figure 3a, the total damping force in engagement behaviors can be expressed as:

$$\begin{aligned}
 F_{tot} &= F_{in} + F_{ed} + F_d = F_{mmr} + F_{gb} + F_{gr} + F_{ed} + F_d \\
 &= (m_{mmr} + m_{gb} + m_{gr})\ddot{x} + (c_{ed} + c_{b1} + c_{b2})\dot{x} + f_{s1} + f_{s2}
 \end{aligned}
 \tag{1}$$

where F_{in} = inertial force; F_{ed} = electromagnetic damping force; F_d = dissipation damping force; F_{mmr} = MMR inertial force; F_{gb} = gearbox inertial force; F_{gr} = generator inertial force; m_{mmr} = the inertia coefficient of the MMR; m_{gb} = the inertia coefficient of the gearbox; m_{gr} = the inertia coefficient of the generator; c_{ed} = the electromagnetic damping coefficient; c_{b1} = the equivalent MMR mechanical damping coefficient; c_{b2} = the equivalent gearbox and generator mechanical damping coefficient; f_{s1} = sliding friction force of the MMR; and f_{s2} = sliding friction force of the gearbox and generator. The dissipative damping force is composed of sliding friction and mechanical damping. Mechanical damping is caused by imprecise workmanship elements, cooperation of parts and energy lost in the generator,

etc. As shown in Figure 3b, the total damping force in disengagement behaviors can be expressed as:

$$F_{tot} = F_{in} + F_d = F_{mmr} + F_d = m_{mmr}\ddot{x} + c_{b1}\dot{x} + f_{s1} \tag{2}$$

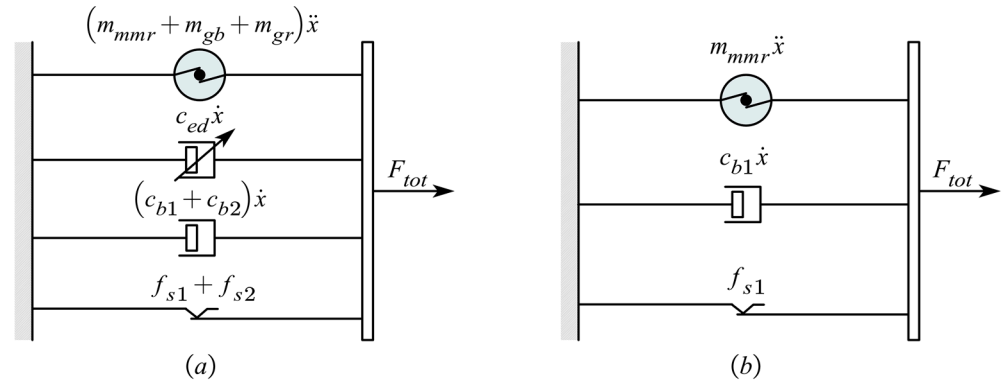


Figure 3. Proposed mechanical models for the MMR–EHSA. (a) Engagement model. (b) Disengagement model.

The inertia coefficient of the MMR in Equations (1) and (2) reads as:

$$m_{mmr} = m_r + \frac{J_{g1}}{r_g^2} + \frac{J_{g2}}{r_g^2} + \frac{J_{g3}}{r_g^2} = m_r + \frac{J_{g1} + J_{g2} + J_{g3}}{r_g^2} \tag{3}$$

where m_r denotes the inertia coefficient of the rack, while J_{g1} , J_{g2} , and J_{g3} represent the inertial parameters of gear 1, gear 2, and gear 3, respectively. r_g denotes the gear radius, i.e., gear 1, gear 2, and gear 3 have the same size. The inertia coefficient of the gearbox is expressed below:

$$m_{gb} = \frac{1}{r_g^2} \left(J_c + \sum_{n=1}^g \frac{J_n}{\prod_{s=1}^n i_s^2} \right) \tag{4}$$

where J_c is the sum rotational inertia of shaft 1 and the coupling. J_n is the rotational inertia of gear n in the gearbox. g is the number of gears in the gearbox. i_s denotes the transmission ratio between gear s and gear 1. The inertia coefficient of the generator can be expressed as:

$$m_{gr} = \frac{J_{gr}}{i_{gb}^2 r_g^2} \tag{5}$$

where J_{gr} denotes the rotational inertia of the generator. i_{gb} denotes the transmission ratio of the gearbox. The rotation of the generator will generate the electromagnetic damping force. The electromagnetic damping coefficient can be expressed as:

$$c_{ed} = \frac{k_e k_t}{(R_{coil} + R_{load}) i_{gb}^2 r_g^2} \tag{6}$$

where k_t and k_e represent the torque constant and the back electromotive voltage constant, respectively. R_{coil} and R_{load} represent the coil resistance of the generator and the load resistance of the generator, respectively. Other parameters (c_{b1} , c_{b2} , f_{s1} , f_{s2}) obtained by the experiments are listed in Table 1. Incidentally, the total damping coefficient of the MMR–EHSA is given by:

$$C = \frac{W}{2f\pi^2 A^2} \tag{7}$$

where W denotes the work of F_{tot} . f denotes the frequency. A denotes the amplitude.

3.2. Numerical Iterative Motion Bifurcation Model of MMR–EHSAs

A novel numerical iteration motion bifurcation model for the nonlinear transmission characterization of MMR–EHSAs is built in this section. This numerical iteration model has two functions. Function 1 is used to judge engagement behavior and disengagement behavior. Function 2 obtains the velocity (\dot{x}) and acceleration (\ddot{x}) of Equations (1) and (2). It has advantages when solving complex excitation input, especially random vibration input. Coupling velocity can represent the characteristics of the disengagement behavior. However, coupling velocity is unknown due to motion bifurcation behavior. Therefore, coupling velocity needs to be calculated. The current moment velocity of the rack is known, and the current moment velocity of coupling can be predicted. Thus, the working behavior of the MMR can be confirmed by comparing the equivalent velocity of the rack and the virtual velocity of the coupling. To sum up, there are three steps:

Step 1: calculate the acceleration of the coupling at the current moment (t_0).

Step 2: calculate the virtual velocity of the coupling in the next moment (t_1) based on the acceleration of the coupling in the current moment (t_0).

Step 3: compare the equivalent velocity of the rack at the next moment (t_1) with the virtual velocity of the coupling (t_1).

The judgment condition for the disengagement behavior is virtual velocity greater than the equivalent rack velocity. Furthermore, virtual velocity less than the equivalent rack velocity is the engagement behavior. The equivalent rack velocity and coupling acceleration can be expressed as:

$$\dot{\theta}_{in} = \left| \frac{v_r}{r_g} \right| \tag{8a}$$

$$\ddot{\theta}_c = \frac{k_e k_t \dot{\theta}_{gr}}{R_{tot} i_{gb}} + M_{fr} \tag{8b}$$

where $\dot{\theta}_{in}$ denotes the equivalent rack velocity; v_r denotes excitation velocity; $\ddot{\theta}_c$ denotes the acceleration of the coupling; and $\dot{\theta}_{gr}$ denotes generator velocity. M_{fr} denotes the equivalent gearbox and generator dissipation damping torque. The virtual velocity of the coupling at the next moment can be calculated using the acceleration of the coupling at the current moment:

$$\dot{\theta}_c = \dot{\theta}_{c0} - \ddot{\theta}_c \Delta t \tag{9}$$

where $\dot{\theta}_{c0}$ represents the initial velocity of the coupling and Δt denotes step length. The iteration process is shown in Table 2.

Table 2. Numerical iterative motion bifurcation model.

Time	Input	Coupling Virtual Velocity	Bifurcation Threshold	Coupling Velocity	Coupling Acceleration
t_0	$\dot{\theta}_{in0}$	$\dot{\theta}_{c0} = 0$	$\begin{cases} \dot{\theta}_{in0} > \dot{\theta}_{c0} \text{ engage} \\ \dot{\theta}_{in0} \leq \dot{\theta}_{c0} \text{ disengage} \end{cases}$	$\begin{cases} \dot{\theta}_{c0} = \dot{\theta}_{in0} \text{ engage} \\ \dot{\theta}_{c0} = \dot{\theta}_{c0} \text{ disengage} \end{cases}$	$\ddot{\theta}_{c0} = \frac{k_e k_t \dot{\theta}_{gr0}}{m_{gb} + m_{gr}} + M_{fr}$
t_1	$\dot{\theta}_{in1}$	$\dot{\theta}_{c1} = \dot{\theta}_{c0} - \ddot{\theta}_{c0} \Delta t$	$\begin{cases} \dot{\theta}_{in1} > \dot{\theta}_{c1} \text{ engage} \\ \dot{\theta}_{in1} \leq \dot{\theta}_{c1} \text{ disengage} \end{cases}$	$\begin{cases} \dot{\theta}_{c1} = \dot{\theta}_{in1} \text{ engage} \\ \dot{\theta}_{c1} = \dot{\theta}_{c1} \text{ disengage} \end{cases}$	$\ddot{\theta}_{c1} = \frac{k_e k_t \dot{\theta}_{gr1}}{m_{gb} + m_{gr}} + M_{fr}$
t_n	$\dot{\theta}_{inn}$	$\dot{\theta}_{cn} = \dot{\theta}_{c(n-1)} - \ddot{\theta}_{c(n-1)} \Delta t$	$\begin{cases} \dot{\theta}_{inn} > \dot{\theta}_{cn} \text{ engage} \\ \dot{\theta}_{inn} \leq \dot{\theta}_{cn} \text{ disengage} \end{cases}$	$\begin{cases} \dot{\theta}_{cn} = \dot{\theta}_{inn} \text{ engage} \\ \dot{\theta}_{cn} = \dot{\theta}_{cn} \text{ disengage} \end{cases}$	$\ddot{\theta}_{cn} = \frac{k_e k_t \dot{\theta}_{grn}}{m_{gb} + m_{gr}} + M_{fr}$

According to Table 2, the motion bifurcation threshold of the MMR–EHSA and the coupling velocity in different behaviors can be obtained. Coupling velocity is synchronous with generator velocity. Generator velocity is obtained from the coupling velocity and the gearbox ratio. It must be pointed out that the coupling is stationary at the initial moment, thus the rotational velocity is zero. No matter what kind of excitation is input, the

MMR–EHSA is always in the engagement behavior at the moment of t_0 . The proposed model has significant universality, and different types of vibration input will not change the difficulty of solving the model. Figure 4 shows the displacement–force curve obtained through the proposed nonlinear dynamics model under harmonic excitation.

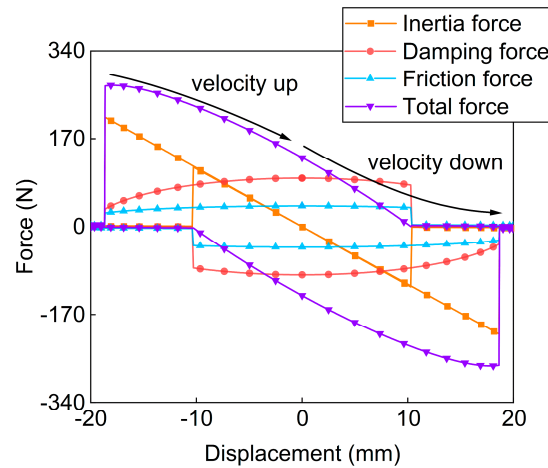


Figure 4. The force–displacement loops of different forces with sinusoidal displacement input. Parameters of input: $A = 20$ mm, $f = 1.0$ Hz, $R_{load} = 20$ Ω .

3.3. Analytical Motion Bifurcation Model of MMR–EHSA

Harmonic excitation is often used as the simulation input when investigating the dynamic characterization of MMR–EHSA [18,19,34]. In this section, the engagement and disengagement behaviors of the EHSA are also calculated using the analytical dynamics model. The equation of harmonic excitation is:

$$\begin{cases} x = A \sin(\omega t) \\ \dot{x} = A\omega \cos(\omega t) \\ \ddot{x} = -A\omega^2 \sin(\omega t) \end{cases} \quad (10)$$

where A represents the amplitude; ω is the angular frequency ($\omega = 2\pi f$); and f denotes the frequency. The force balance condition of the motion bifurcation behavior is the F_{tot} value in the engagement that is equal to the F_{tot} value in the disengagement. The equation can be expressed as:

$$(m_{mmr} + m_{gb} + m_{gr})\ddot{x} + (c_{ed} + c_{b2})\dot{x} + f_{s2} = 0 \quad (11)$$

Using the auxiliary angle formula, Equation (11) can be expressed as:

$$\begin{aligned} \sqrt{a^2 + b^2} \cos(\omega t_{dis} - \arctan\left(\frac{b}{a}\right)) + f_{s2} &= 0 \\ \begin{cases} a = -(m_{mmr} + m_{gb} + m_{gr})\omega^2 A \\ b = (c_{ed} + c_{b2})\omega A \end{cases} \end{aligned} \quad (12)$$

Solving Equation (12) can obtain the bifurcation threshold:

$$t_{dis} = \frac{1}{2\pi f} \left[\arccos\left(-\frac{f_{s2}}{\sqrt{a^2 + b^2}}\right) + \arctan\left(\frac{b}{a}\right) \right] \quad (13)$$

In a cycle of harmonic excitation, Equation (13) has two solutions. The two solutions differ by half a cycle. The coupling velocity in the disengagement behavior is expressed as:

$$\dot{\theta}_{cn} = \dot{\theta}_{c(n-1)} \left(1 - \frac{k_e k_t \Delta t}{i_{gb}^2 (m_{gb} + m_{gr})}\right) - \frac{M_{c2(n-1)} \Delta t}{(m_{gb} + m_{gr})} \quad (14a)$$

$$\dot{\theta}_c = \dot{\theta}_{c0} \exp\left(-\frac{m_e}{c_e} t\right) \quad (14b)$$

Equation (14a) is the iterative model proposed in this paper, which can also be coupled to an analytical dynamics model. Equation (14b) [35] is the velocity attenuation equation in the disengagement behavior, where m_e is the inertia coefficient in the disengagement behavior and c_e is the equivalent damping coefficient in the disengagement behavior. The following engagement moment can be solved using the numerical iterative method:

$$t_{en} = t_{dis} + h\Delta t \quad (15)$$

where h is the number of iterations when $\dot{\theta}_c$ is the same as excitation velocity. The analytical method needs to transform the excitation signal into the superposition of harmonic function through Fourier transformation and then needs to solve the bifurcation threshold according to the auxiliary angle formula. Many excitation inputs, in reality, tend to be random. The analytic method cannot get the exact input function when solving random input, which makes the solution difficult.

3.4. Quantitative Power Flow Model of MMR–EHSA

The MMR–EHSA power flow model can help in understanding vibrational energy dissipation and the energy harvesting process. The key to establishing the quantitative power flow model is to calculate the threshold of MMR–EHSA motion bifurcation. This is because the power generated by MMR–EHSA is different in engagement and disengagement.

Figure 5 shows power flow in the engagement behavior. The engagement power flow equation is:

$$\begin{aligned} P_{in} &= P_{md} + P_{gd} + P_{mi} + P_{gi} + P_{ge} = P_{md} + P_{gd} + P_{mi} + P_{gi} + P_{tot} \\ &= P_{md} + P_{gd} + P_{mi} + P_{gi} + P_{el} + P_{eout} \end{aligned} \quad (16)$$

where P_{in} = power of total damping force; P_{md} = equivalent power of MMR dissipation damping force; P_{gd} = equivalent power of gearbox and generator dissipation damping force; P_{mi} = power of MMR inertia force; P_{gi} = power of gearbox and generator inertia force; P_{ge} = power of electromagnetic damping force; P_{tot} = gross output power; P_{el} = power of copper coil loss; and P_{eout} = output power. Figure 6 shows the power flow in disengagement behavior. The disengagement power flow equation is:

$$P_{in} = P_{md} + P_{mi} \quad (17a)$$

$$P_{gi} = P_{gd} + P_{ge} = P_{gd} + P_{tot} = P_{gd} + P_{el} + P_{eout} \quad (17b)$$

As shown in Figure 6, Equation (17a) represents external power flow. Only the MMR produces damping forces in the disengagement behavior. Equation (17b) represents internal power flow. The internal power flow releases the accumulated kinetic energy in the engagement behavior. The kinetic energy of the gearbox and the generator rotor drive themselves to rotate. Due to roller clutch disengagement, the generator and gearbox do not provide damping force.

The cumulative effect of total inertia force is zero for an EHSA without an MMR in a harmonic excitation cycle. However, the cumulative effect of inertia force produced by MMR–EHSA needs to be classified. Firstly, the average power generated by the inertia force of an MMR in a cycle is zero, as shown in the following equation.

$$P_{mi} = \frac{1}{T} m_{mmr} \int_0^T \ddot{x}\dot{x} dt = 0 \quad (18)$$

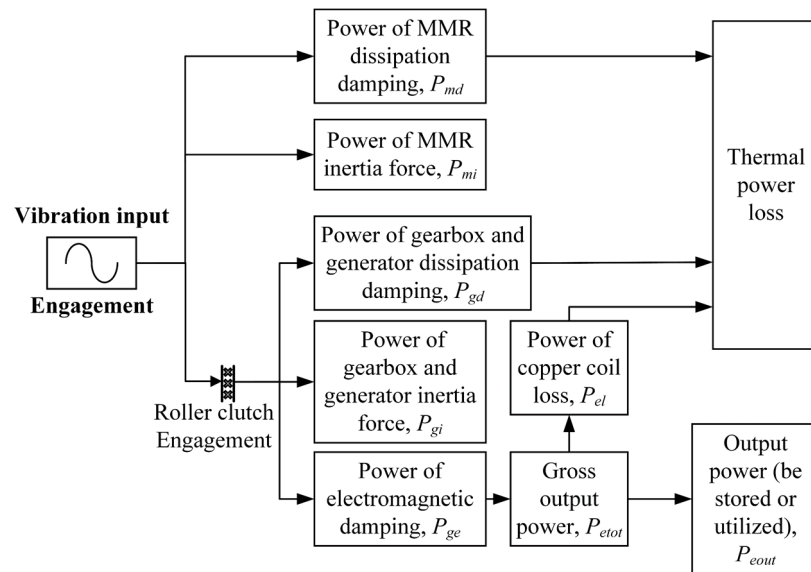


Figure 5. The power flow of the engagement behavior.

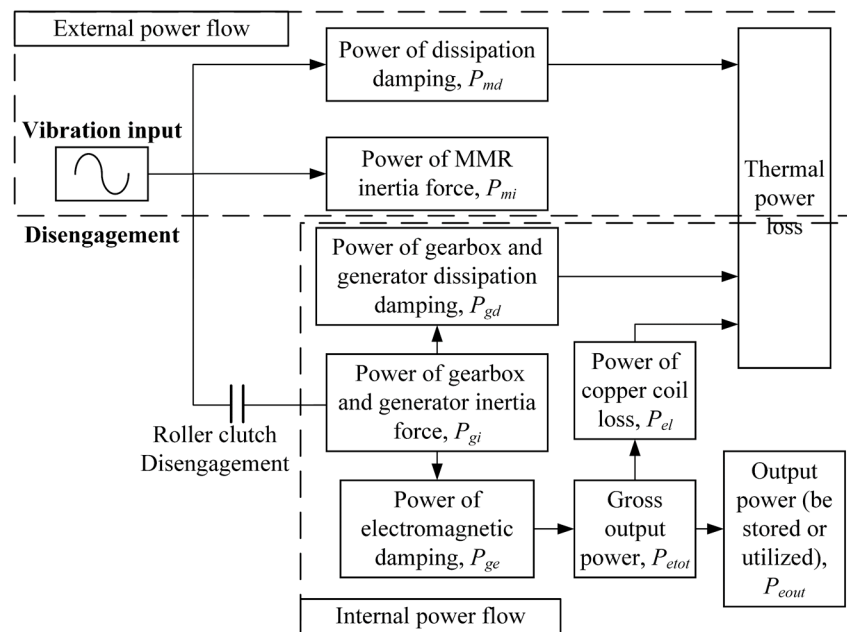


Figure 6. The power flow of the disengagement behavior.

Secondly, the average power of inertia force, electromagnetic damping force, and dissipation damping force for the gearbox and the generator can be expressed as:

$$P_{gi} = \frac{1}{T} (m_{gb} + m_{gr}) r_p^2 \int_0^T \ddot{\theta}_{gr}(t) \dot{\theta}_{gr}(t) dt \tag{19}$$

$$P_{ge} = \frac{1}{T} c_{ed} r_p^2 \int_0^T \dot{\theta}_{gr}^2(t) dt \tag{20}$$

$$P_{gd} = \frac{1}{T} r_p \int_0^T f_s(t) \dot{\theta}_{gr}(t) dt + \frac{1}{T} r_p^2 \int_0^T c_b(t) \dot{\theta}_{gr}^2(t) dt \tag{21}$$

where $\dot{\theta}_{gr}$ and $\ddot{\theta}_{gr}$ can be acquired by the proposed numerical iterative dynamics model. The average power of engagement behavior and disengagement behavior can be expressed as:

$$P_{gien} = \frac{1}{z} \sum_{k=1}^z \frac{1}{(t_{disk} - t_{enk})} (m_{gb} + m_{gr}) r_p^2 \int_{t_{enk}}^{t_{disk}} \ddot{\theta}_{gr}(t) \dot{\theta}_{gr}(t) dt \quad (22)$$

$$P_{gidis} = \frac{1}{z} \sum_{k=1}^z \frac{1}{(t_{en(k+1)} - t_{disk})} (m_{gb} + m_{gr}) r_p^2 \int_{t_{disk}}^{t_{en(k+1)}} \ddot{\theta}_{gr}(t) \dot{\theta}_{gr}(t) dt \quad (23)$$

$$P_{geen} = \frac{1}{z} \sum_{k=1}^z \frac{1}{(t_{disk} - t_{enk})} c_{ed} r_p^2 \int_{t_{enk}}^{t_{disk}} \dot{\theta}_{gr}^2(t) dt \quad (24)$$

$$P_{gedis} = \frac{1}{z} \sum_{k=1}^z \frac{1}{(t_{en(k+1)} - t_{disk})} c_{ed} r_p^2 \int_{t_{disk}}^{t_{en(k+1)}} \dot{\theta}_{gr}^2(t) dt \quad (25)$$

$$P_{gden} = \frac{1}{z} \sum_{k=1}^z \frac{r_p}{(t_{disk} - t_{enk})} \left(\int_{t_{enk}}^{t_{disk}} f_s(t) \dot{\theta}_{gr}(t) dt + r_p \int_{t_{enk}}^{t_{disk}} c_b(t) \dot{\theta}_{gr}^2(t) dt \right) \quad (26)$$

$$P_{gddis} = \frac{1}{z} \sum_{k=1}^z \frac{r_p}{(t_{en(k+1)} - t_{disk})} \left(\int_{t_{disk}}^{t_{en(k+1)}} f_s(t) \dot{\theta}_{gr}(t) dt + r_p \int_{t_{disk}}^{t_{en(k+1)}} c_b(t) \dot{\theta}_{gr}^2(t) dt \right) \quad (27)$$

where P_{gien} = average power of inertia force in engagement; P_{gidis} = average power of inertia force in disengagement; P_{geen} = average power of electromagnetic damping force in engagement; P_{gedis} = average power of electromagnetic damping force in disengagement; P_{gden} = average power of dissipation damping force in engagement; P_{gddis} = average power of dissipation damping force in disengagement; t_{enk} = the moment of k engagement; t_{disk} = the moment of k disengagement; $t_{en(k+1)}$ = the moment of $k + 1$ engagement; and z = the number of occurring motion bifurcation behaviors. The voltage generated by the generator is related to the velocity, which can be expressed as:

$$u_0 = k_e \dot{\theta}_{gr} \quad (28)$$

Open circuit current can be expressed as:

$$i_0 = \frac{u_0}{R_{coil} + R_{load}} \quad (29)$$

Generator coil voltage and generator output voltage are expressed as:

$$u_{coil} = \frac{R_{coil}}{R_{coil} + R_{load}} u_0 \quad (30)$$

$$u_{load} = \frac{R_{load}}{R_{coil} + R_{load}} u_0 \quad (31)$$

The average coil power is expressed as:

$$P_{el} = \frac{1}{T} \int_0^T \frac{(k_e \dot{\theta}_{gr})^2 R_{coil}}{(R_{coil} + R_{load})^2} dt = \frac{1}{T} \frac{k_e^2 R_{coil}}{(R_{coil} + R_{load})^2} \int_0^T \dot{\theta}_{gr}^2 dt \quad (32)$$

$$P_{elen} = \frac{1}{z} \sum_{k=1}^z \frac{1}{(t_{disk} - t_{enk})} \frac{k_e^2 R_{coil}}{(R_{coil} + R_{load})^2} \int_{t_{enk}}^{t_{disk}} \dot{\theta}_{gr}^2 dt \quad (33)$$

$$P_{eldis} = \frac{1}{z} \sum_{k=1}^z \frac{1}{(t_{en(k+1)} - t_{disk})} \frac{k_e^2 R_{coil}}{(R_{coil} + R_{load})^2} \int_{t_{disk}}^{t_{en(k+1)}} \dot{\theta}_{gr}^2 dt \quad (34)$$

where P_{elen} denotes the average coil power in engagement and P_{eldis} denotes the average coil power in disengagement. The average output power is expressed as:

$$P_{eout} = \frac{1}{T} \int_0^T \frac{(k_e \dot{\theta}_{gr})^2 R_{load}}{(R_{coil} + R_{load})^2} dt = \frac{1}{T} \frac{k_e^2 R_{load}}{(R_{coil} + R_{load})^2} \int_0^T \dot{\theta}_{gr}^2 dt \quad (35)$$

$$P_{eouten} = \frac{1}{z} \sum_{k=1}^z \frac{1}{(t_{disk} - t_{enk})} \frac{k_e^2 R_{load}}{(R_{coil} + R_{load})^2} \int_{t_{enk}}^{t_{disk}} \dot{\theta}_{gr}^2 dt \quad (36)$$

$$P_{eoutdis} = \frac{1}{z} \sum_{k=1}^z \frac{1}{(t_{en(k+1)} - t_{disk})} \frac{k_e^2 R_{load}}{(R_{coil} + R_{load})^2} \int_{t_{disk}}^{t_{en(k+1)}} \dot{\theta}_{gr}^2 dt \quad (37)$$

where P_{eouten} denotes the average output power in engagement and $P_{eoutdis}$ denotes the average output power in disengagement.

4. Test Bench

4.1. Experimental Setup

Figure 7a shows the prototype MMR–EHSA designed and fabricated for dynamic testing. The generator is a necessary part of the MMR–EHSA. Different generators will directly affect the performance of MMR–EHSA. The generator used in this paper contains a gearbox. It can increase the speed of the generator rotor. The transmission ratio is an important parameter. It will affect improvements in generator speed. If generator speed is increased by too little, energy harvesting will be reduced but the transmission of the MMR–EHSA will be more stable. If generator speed is increased by too much, harvesting power will be improved but transmission stability will deteriorate. Therefore, a large number of experiments are needed before selecting the appropriate generator in order to preliminarily match the appropriate generator. The generator used in this paper is manufactured by XingDa Company (Model: XD775 200R). Figure 7b shows the bench manufactured by LIANGONG TESTING company (Model: TPJ-W5A). This bench can test the damping characteristics of the shock absorber. Figure 7c demonstrates the device used to test voltages. The collected force signal and voltage signal are shown in Figure 7d.

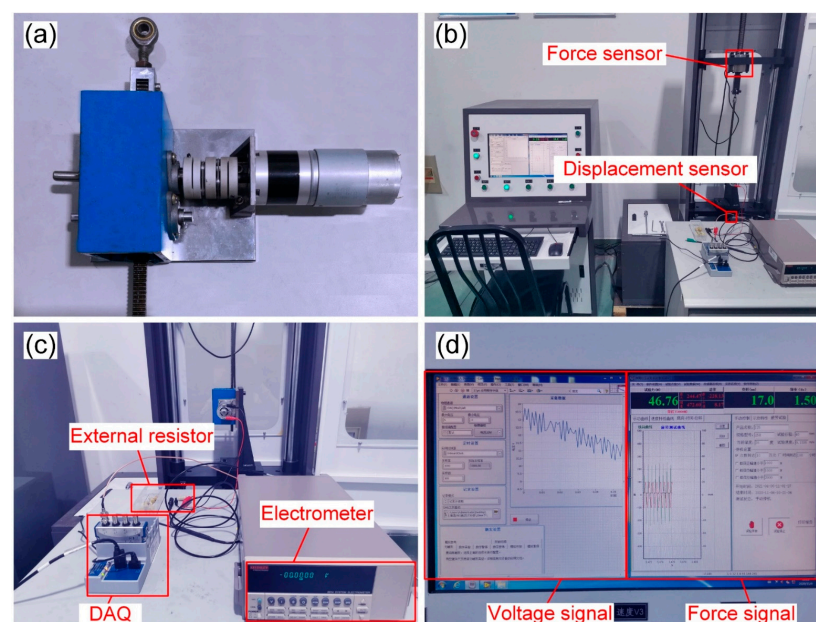


Figure 7. Lab testing. (a) EHSA prototype. (b) Dynamic test. (c) Electric test. (d) Voltage signal and force signal.

4.2. Experimental Results and Analysis

The MMR–EHSA has two kinds of work states. However, the two work states do not appear together in some excitation conditions. As a result, we chose testing amplitudes of 20 mm and 30 mm with frequencies of 0.5 Hz and 1.0 Hz. A set of resistors (5 Ω , 10 Ω , 20 Ω , 50 Ω) were used in the dynamic testing. Two kinds of working characteristic were achieved as a result. One is motion bifurcation including engagement and disengagement. The other is engagement only. Figure 8 shows the test and simulation results. The area enclosed by each curve in Figure 8a,b represents the vibrational energy dissipated by the MMR–EHSA in a loading cycle. The load resistance is small and the area enclosed is large because the small load resistance leads to a larger electromagnetic damping force. As shown in Figure 8a, motion bifurcation occurs when the load resistance is 20 Ω and 50 Ω . The damping force is very small in the disengagement area. In Figure 8b, the MMR–EHSA is always in an engagement state due to low excitation frequency. The output voltage results are shown in Figure 8c,d, with 0– $T/2$ s being the measured results and $T/2$ – T s being the simulation results.

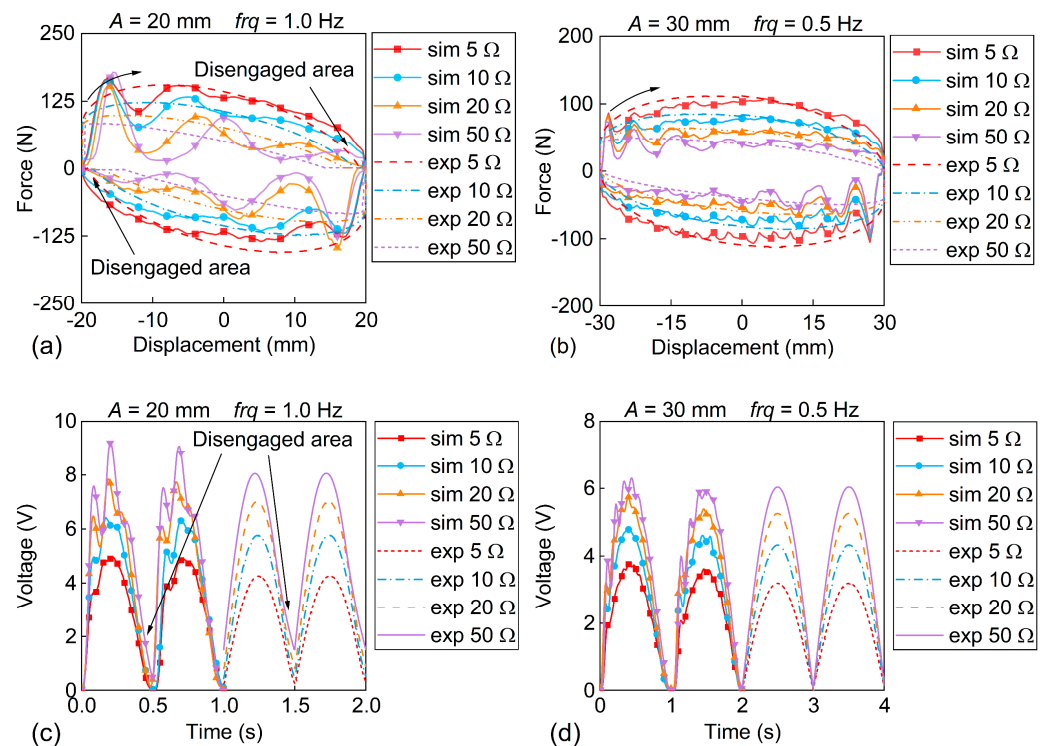


Figure 8. Simulation and experiment. (a) Total force ($A = 20$ mm, $f = 1.0$ Hz). (b) Total force ($A = 30$ mm, $f = 0.5$ Hz). (c) Voltage ($A = 20$ mm, $f = 1.0$ Hz). (d) Voltage ($A = 30$ mm, $f = 0.5$ Hz).

It should be noted that the simulation results are smooth, while the experimental results fluctuate. This fluctuation phenomenon makes the simulation inconsistent with the experimental results, especially at 50 Ω . The reason for this is as follows. According to Equation (28), voltage is linearly related to generator velocity. Therefore, generator velocity fluctuates based on Figure 8c, and the fluctuant velocity is higher than the input velocity. The gear meshing impact and the stiffness of transmission parts lead to velocity fluctuation. The transmission parts will produce elastic deformation and accumulate elastic potential energy during acceleration. The elastic potential energy will be released with the decrease in acceleration velocity, thus increasing the velocity of the generator and making the EHSA undergo motion bifurcation in the acceleration phase. However, motion bifurcation in the acceleration phase will quickly terminate. The transmission parts will then continue to produce elastic deformation which increases generator velocity. The experimental results have the same trend as the simulation results. In addition, the damping force and output

voltage can be changed by adjusting load resistance. Furthermore, it must be pointed out that the working characteristic in a cycle should be focused on because the MMR–EHSA is required to work for a long period of time. As shown in Figure 9, the total force power and the output power agree with the experimental and simulated results in a cycle. This proves that the nonlinear dynamics model proposed is effective.

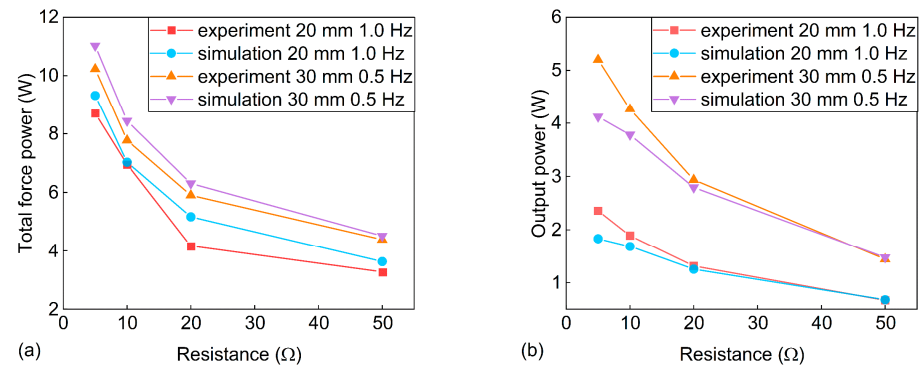


Figure 9. Simulation and experiment in a cycle. (a) Total force power. (b) Energy harvesting output power.

5. Quantitative Power Flow Discussion

The quantitative power flow of MMR–EHSA is discussed in this section. General vibrations can be transformed into a superposition of harmonic functions through Fourier transformation. The operating characteristics under harmonic excitation are the basis for the study of MMR–EHSA. Unlike the power flow analysis of MMR–EHSA in other studies [18], power flow in this paper is divided into engagement power and disengagement power according to the motion bifurcation threshold. This allows for a more accurate analysis of power changes and discoveries. In addition, Section 5.3 first discusses the power of random excitation input. The advantages of the proposed numerical iterative model in the study of random vibration input are justified.

5.1. Quantitative Power Flow Analysis within a Harmonic Cycle

This section shows the influence of motion bifurcation on the different forces of power in harmonic excitation. Figure 10a shows the total force power for dissipating the input vibrational energy. Total force power is a combination of MMR inertial force (Figure 10b), MMR dissipation damping force (Figure 10c), inertial (Figure 10d) and dissipation damping forces (Figure 10e) generated by the generator and gearbox, and electromagnetic damping force (Figure 10f). The generator’s inertial force, dissipation damping force, and electromagnetic damping force cannot be transferred to the rack when motion bifurcation occurs. This results in minimal power in Regions A and B. At the same time, Region C has a double peak. This double peak makes the power generated by the total force at 0.5 s smooth, which is beneficial for the dissipation of vibrational energy. The MMR does not undergo motion bifurcation and is always in the engagement state. The accumulated effect of MMR inertial force in a cycle of harmonic excitation is zero. In Figure 10d, the generator’s inertial force also generates power in disengagement. The generator’s rotor drives generator rotation in the disengagement state, releasing the kinetic energy of the generator rotor accumulated in the engagement state. The dissipation damping force of the generator and gearbox and the electromagnetic damping force consume the kinetic energy.

5.2. Average Power Analysis of Different Resistances

The MMR–EHSA consumes vibrational energy and harvests electrical energy affected by motion bifurcation. The engagement and disengagement states are related to input vibration and load resistance. The former is often uncontrollable, while the latter can be controlled. Figure 11a shows the total damping forces with different resistances under harmonic excitation. The motion bifurcation threshold can be distinguished and acquired

using the nonlinear dynamics model or calculated by Equations (13) and (15). The force change is nonlinear as the resistance changes. A slight change in resistance brings a significant change in force when the resistance is less than 10Ω , whereas the force changes flatly after resistance is greater than 10Ω . The moment of entering the disengagement state is advanced by 0.092 s during the change in resistance from 1Ω to 50Ω . In contrast, the moment of entering the engagement state lags by 0.23 s . The resistance change affects the moment of disengagement more than that of the engagement moment under harmonic excitation. Figure 11b shows the coupling velocity at different resistances. The coupling velocity change is continuous during motion bifurcation. The velocity changes abruptly when motion bifurcation occurs. Therefore, the engagement moment is clear, and the disengagement moment is blurred.

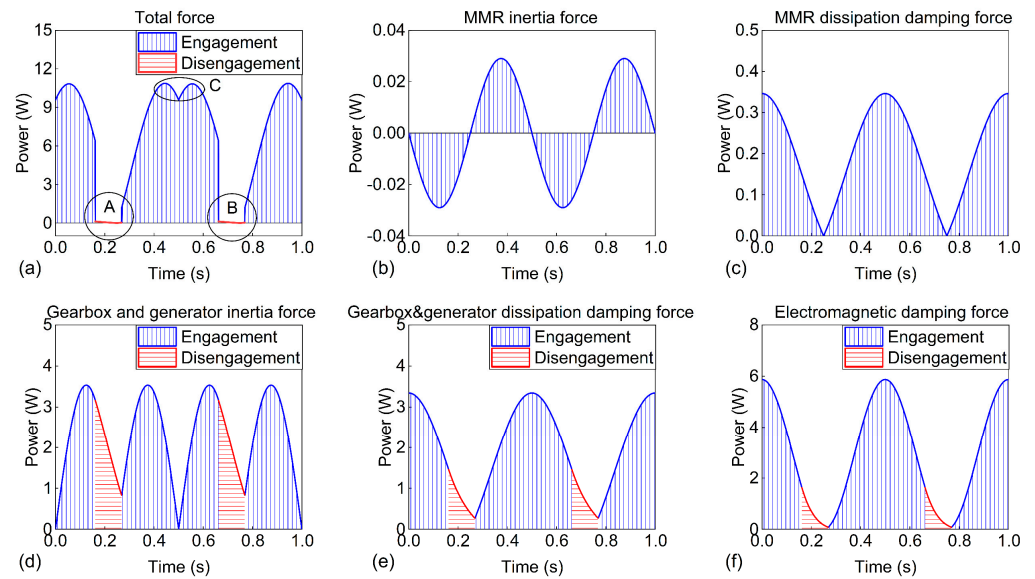


Figure 10. Different force powers (parameters of input: $A = 20 \text{ mm}$, $f = 1.0 \text{ Hz}$, $R_{load} = 20 \Omega$). (a) Total force power. (b) MMR inertia force power. (c) MMR dissipation damping force power. (d) Gearbox and generator inertia force power. (e) Gearbox and generator dissipation damping force power. (f) Damping force power.

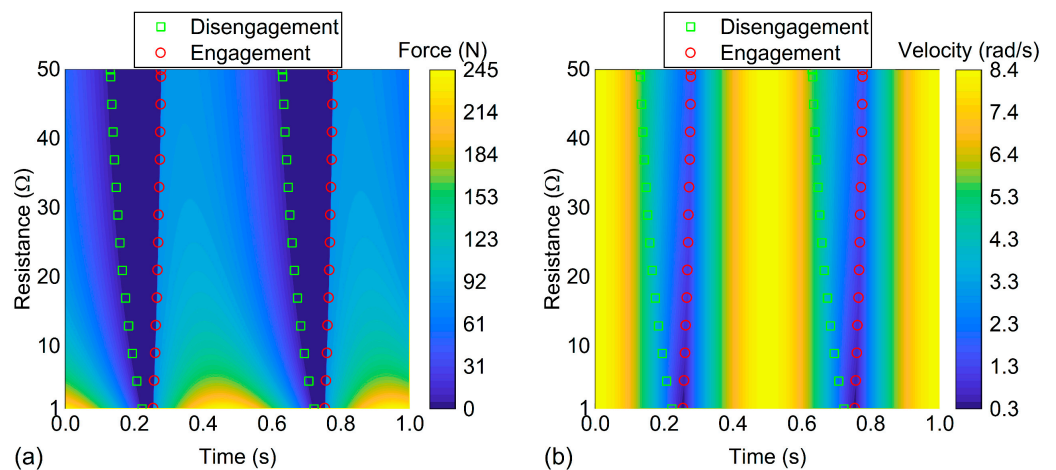


Figure 11. The working characterization of the MMR–EHSA with different resistances (parameters of input: $A = 20 \text{ mm}$, $f = 1.0 \text{ Hz}$, $R_{load} = 1\text{--}50 \Omega$). (a) Total damping force. (b) Coupling velocity.

Figure 12 discusses the average power in different states according to the bifurcation threshold. In Figure 12a,b, the average powers of the inertial force and dissipation damping force generated by the gearbox and generator are shown. There is a decrease in the engagement state and an increase in the disengagement state with external resistance. Furthermore, this variation law increases with excitation frequency. Figure 12c is the average power of the electromagnetic damping force, which is related to the load resistance in Equation (6). The increase in resistance will cause a sharp decrease in electromagnetic damping force. At the same time, the duration of the disengagement state is increasing, as shown in Figure 11. As a joint result, the power of the disengagement state decreases continuously, and that of the engagement state changes slowly. Figure 12d is the average power of the total damping force. Only the MMR inertia force and dissipation damping force provide damping force in the disengagement state, resulting in almost 0 W of power. The power of engagement damping force decreases with increases in load resistance. A slight change in resistance will cause a significant change in power when the resistance is less than 10 Ω. The power changes slowly with increasing resistance when the resistance is greater than 10 Ω. To sum up, it is difficult to control the damping power of EHSA's when the resistance is smaller than 10 Ω. In addition, when load resistance is approximately 0 Ω, the maximum damping power will be reached.

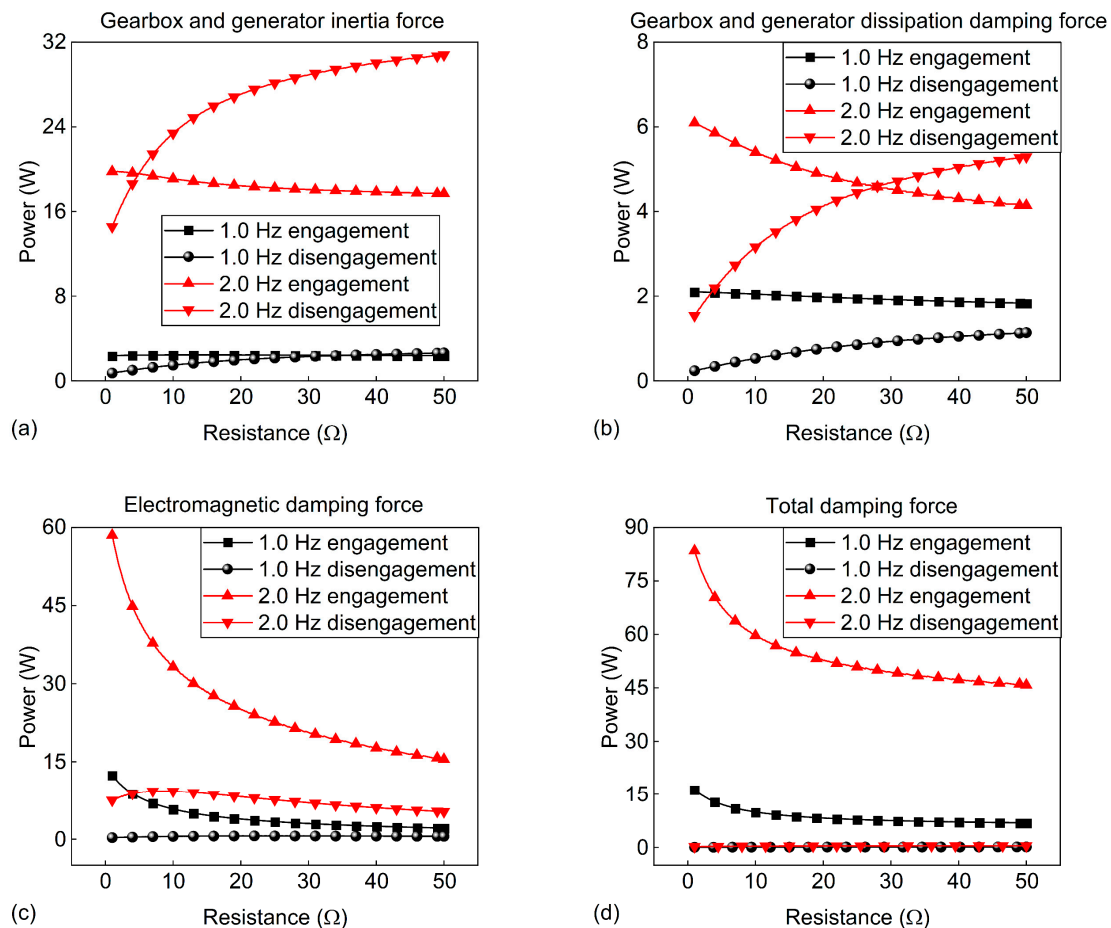


Figure 12. Different force powers with different resistances (parameters of input: $A = 20$ mm). (a) Power of the inertial force of the gearbox and the generator. (b) Gearbox and generator dissipation damping force. (c) Electromagnetic damping force. (d) Total damping force.

Figure 13a compares the output power with the coil power. According to Equations (32) and (35), the necessary condition for P_{eout} to be equal to P_{el} is $R_{load} = R_{coil}$. Therefore, the value of coil resistance (5.5 Ω) is the intersection ($P_{eout} = P_{el}$) of output power and coil power. The increase in load resistance makes coil power decrease sharply. Simultaneously, there is

an optimal load resistance value for maximizing output power. The optimal load resistance for maximum energy harvesting is the coil resistance for the EHSA without an MMR [24]. However, it must be noted that coil resistance may not be the resistance of maximum energy harvesting output power for an MMR–EHSA. The maximum output resistance will change with frequency. Table 3 shows the change for output power with different load resistances. The point where maximum output power at 1.0 Hz is reached is 5.5Ω . However, the point where maximum output power is reached for 2.0 Hz is 6.0Ω . This phenomenon is caused by motion bifurcation, which is generated by the MMR. The MMR improves the energy harvesting capacity of the EHSA [36], but also makes the harvesting process more complex. Through the proposed dynamics model, the maximum output resistance can be revealed. Figure 13b shows coil power at different states. Coil power decreases with increases in resistance for both the engagement state and disengagement state. Furthermore, when the load resistance is greater than 20Ω , coil power reaches a very flat state. Figure 13c shows the output power in different states. The resistance point for maximum output power is different in the engagement state and disengagement state. Therefore, it is necessary to consider motion bifurcation when optimizing MMR–EHSAs in the future. Meanwhile, energy harvesting and damping force will affect each other. It is difficult to achieve both optimal states at the same time. A reasonable compromise should be made in the selection of load resistance.

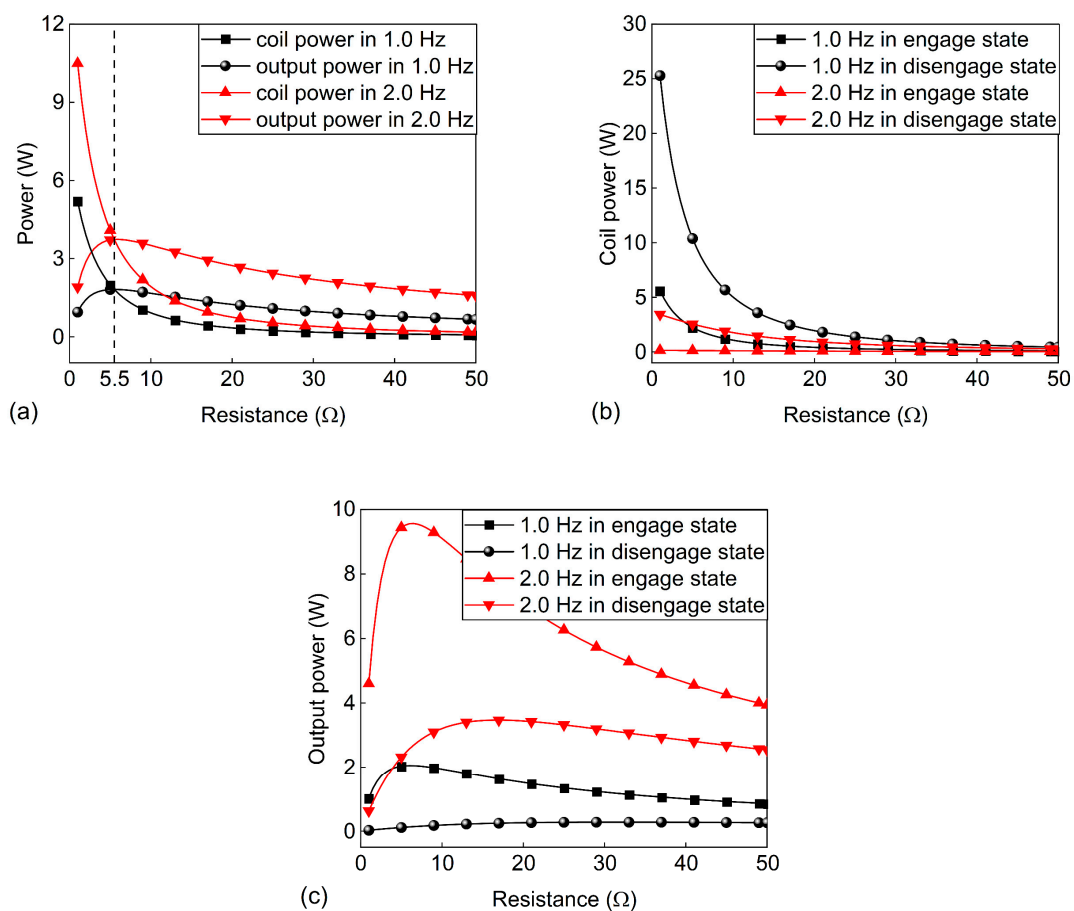


Figure 13. A generator consuming and harvesting power with different resistances (parameters of input: $A = 20 \text{ mm}$). (a) Output power and coil power. (b) Coil power in the engagement state and disengagement state. (c) Output power in the engagement state and disengagement state.

Table 3. Output electrical energy with different load resistances.

	4.5 Ω	5.0 Ω	5.5 Ω	6.0 Ω	6.5 Ω	7.0 Ω
1 Hz	1.8005 W	1.8148 W	1.8193 W	1.8161 W	1.8073 W	1.7941 W
2 Hz	3.6810 W	3.7190 W	3.7369 W	3.7396 W	3.7306 W	3.7307 W

5.3. The Theoretical Model Solves for Random Vibration

In application, the environment often provides random excitation to MMR–EHSA. A theoretical model that can solve random excitation is needed, which could help performance evaluation during the MMR–EHSA design process as a result. Compared to the existing model [6], the proposed numerical iteration nonlinear dynamics model has advantages when solving random vibration inputs. Different types of vibration input do not increase the difficulty of solving the model. This section shows the results of solutions for MMR–EHSA subjected to random vibrations that prove the solving ability of the proposed model. The random vibration input is set as a filtered white noise function:

$$\dot{q}(t) = -2\pi f_0 q(t) + 2\pi \sqrt{S_q(n_0)} u \omega(t) \quad (38)$$

where $q(t)$ denotes the input displacement; f_0 denotes the lower cut-off frequency ($f_0 = 2\pi n_{00} u$); $S_q(n_0)$ denotes the roughness index; u denotes the horizontal movement velocity; and $\omega(t)$ denotes the uniformly distributed white noise with a mean value 0 and intensity of 1. The parameters are listed in Table 1.

Figure 14a shows the random displacement input and Figure 14b shows the nonlinear transmission characteristics of the MMR–EHSA. The velocity of gear 1 and gear 2 corresponds to the input displacement. The coupling velocity is the envelope of the gears in the time domain. It can be seen from the coupling velocity that the shape of the curve is a sawtooth, and the rising edge and falling edge of the sawtooth are the engagement state and disengagement state, respectively. The noise is filtered and the large input displacement signal is saved. This makes energy harvesting more stable. Figure 14c shows the total force generated by the MMR–EHSA. The total force consists of many significant impulses and a considerable amount of slight noise. Each large total force impulse corresponds to the rising edge of coupling velocity. The noise near 0 N is the damping force generated by the disengagement state, which corresponds to the falling edge of coupling velocity. Comparing Figure 14c,d, it is found that the appearing moments of pulse peaks are the same between total force and total force power, while the variation patterns of the pulse peaks in the time domain vary. The peak variation pattern of the total force power and output power pulse peaks is related to the variation of coupling velocity. The rising edge of coupling velocity represents the velocity difference of the generator, which raises the total force power. Furthermore, the generator's rotor is linearly related to coupling velocity, thus generator output power depends on coupling velocity, as shown in Figure 14e. MMR–EHSA may be applied for use in relation to automobiles, traffic, and biology. Mathematical models for the existence of random signals in different domains are known. Through the random input solution method proposed in this paper, the performance of the designed MMR–EHSA can be estimated during the design of the MMR–EHSA.

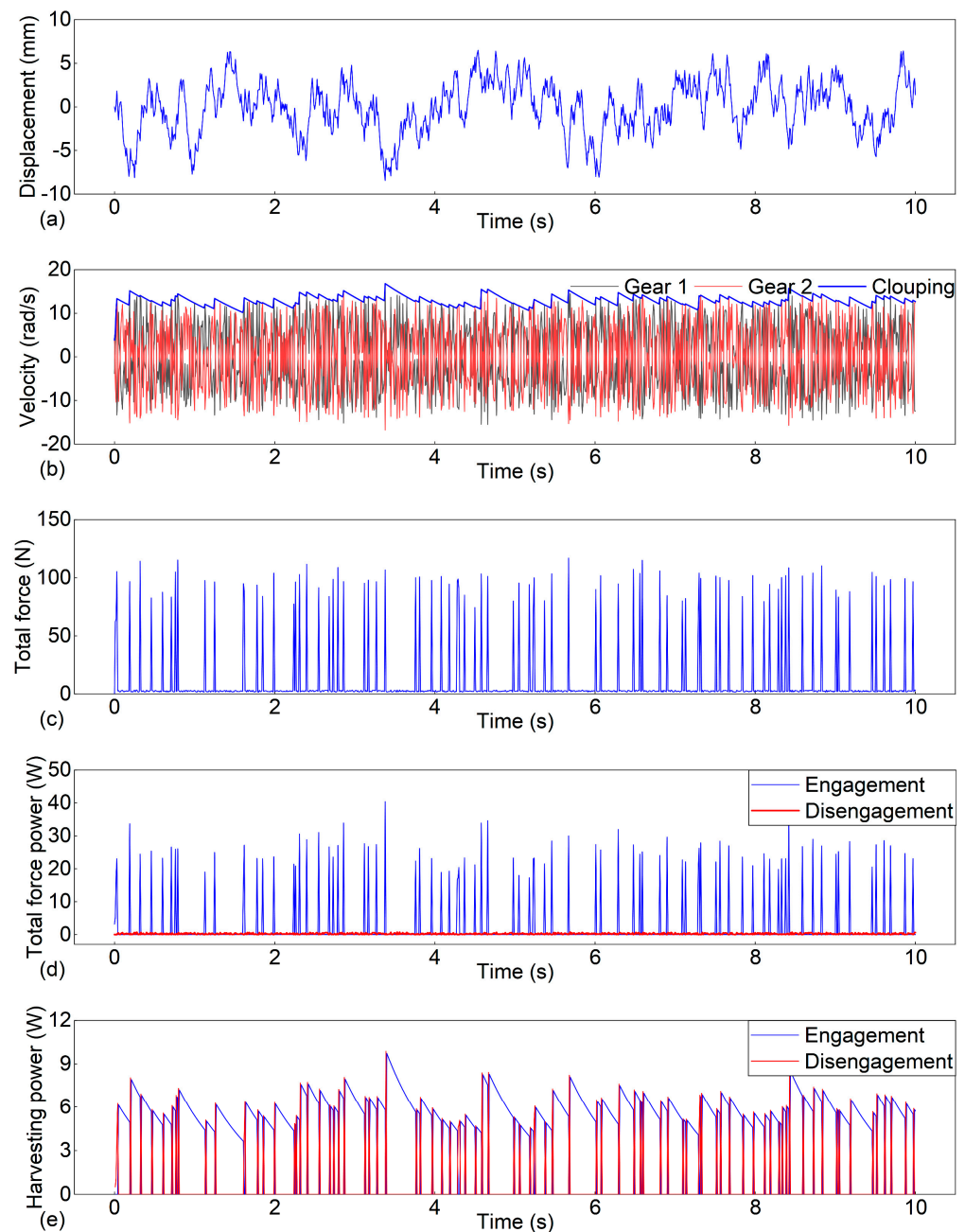


Figure 14. The operating characteristics of an MMR–EHSA subjected to random vibrations. (a) Input displacement. (b) Velocity characterization. (c) Total force. (d) Total force power. (e) Harvesting power.

6. Conclusions

In this paper, a novel nonlinear dynamics model to solve the motion bifurcation threshold of MMR–EHSAs was proposed. The power flow model was established according to the dynamics model. An MMR–EHSA prototype was fabricated. The performance of the MMR–EHSA was tested using bench experiments. The theoretical model can effectively predict the test results. The influence of load resistance on the disengagement duration was studied under harmonic excitation. The disengagement duration increased from 0.092 s to 0.23 s under working conditions where the frequency, amplitude, and resistance were 1.0 Hz, 10 mm, and 1–50 Ω , respectively. Damping force power and energy harvesting power were studied under harmonic excitation. The maximum damping force power appears in the condition where the positive and negative terminals of the generator are short-circuited ($R \approx 0 \Omega$). The optimal energy harvesting power that matches resistance

will change with frequency and amplitude. The optimal energy harvesting resistance value can be solved using the power flow model. In addition, the proposed dynamics model has advantages when solving random vibration input as different types of input do not change the difficulty of finding solutions.

Author Contributions: Conceptualization, J.L. and P.W.; methodology, J.L. and P.W.; software, J.L. and P.W.; validation, J.L., P.W. and D.G.; formal analysis, J.L. and P.W.; investigation, J.L. and S.L.; resources, J.L. and D.G.; data curation, J.L., Y.G. and P.W.; writing—original draft preparation, J.L. and P.W.; writing—review and editing, J.L. and S.L.; visualization, J.L. and P.W.; supervision, J.L., D.G. and S.L.; project administration, J.L., S.L. and D.G.; funding acquisition, D.G. and J.L. All authors have read and agreed to the published version of the manuscript.

Funding: This work was supported by Financial Support of the National Natural Science Foundation of China [Grant No. 52005433], Special Cooperation Foundation for Yangzhou & YZU [No. YZU202102].

Data Availability Statement: The data that support the findings of this study are available from the corresponding author upon reasonable request.

Conflicts of Interest: The authors declare no conflict of interest.

References

1. Bucinskas, V.; Mitrouchev, P.; Sutinyas, E.; Sesok, N.; Iljin, I.; Morkvenaite-Vilkonciene, I. Evaluation of Comfort Level and Harvested Energy in the Vehicle Using Controlled Damping. *Energies* **2017**, *10*, 1742. [\[CrossRef\]](#)
2. Lee, J.; Chun, Y.; Kim, J.; Park, B. An Energy-Harvesting System Using Mppt at Shock Absorber for Electric Vehicles. *Energies* **2021**, *14*, 2552. [\[CrossRef\]](#)
3. Gijón-Rivera, C.; Olazagoitia, J.L. Methodology for Comprehensive Comparison of Energy Harvesting Shock Absorber Systems. *Energies* **2020**, *13*, 6110. [\[CrossRef\]](#)
4. Duong, M.T.; Chun, Y.D.; Hong, D.K. Design of a High-Performance 16-Slot 8-Pole Electromagnetic Shock Absorber Using a Novel Permanent Magnet Structure. *Energies* **2018**, *11*, 3352. [\[CrossRef\]](#)
5. Zou, H.X.; Zhao, L.C.; Gao, Q.H.; Zuo, L.; Liu, F.R.; Tan, T.; Wei, K.X.; Zhang, W.M. Mechanical Modulations for Enhancing Energy Harvesting: Principles, Methods and Applications. *Appl. Energy* **2019**, *255*, 113871. [\[CrossRef\]](#)
6. Zou, H.X.; Li, M.; Zhao, L.C.; Gao, Q.H.; Wei, K.X.; Zuo, L.; Qian, F.; Zhang, W.M. A Magnetically Coupled Bistable Piezoelectric Harvester for Underwater Energy Harvesting. *Energy* **2021**, *217*, 119429. [\[CrossRef\]](#)
7. Qian, J.; Jing, X. Wind-Driven Hybridized Triboelectric-Electromagnetic Nanogenerator and Solar Cell as a Sustainable Power Unit for Self-Powered Natural Disaster Monitoring Sensor Networks. *Nano Energy* **2018**, *52*, 78–87. [\[CrossRef\]](#)
8. Guan, D.; Cong, X.; Li, J.; Shen, H.; Zhang, C.; Gong, J. Quantitative Characterization of the Energy Harvesting Performance of Soft-Contact Sphere Triboelectric Nanogenerator. *Nano Energy* **2021**, *87*, 106186. [\[CrossRef\]](#)
9. Liang, C.; Ai, J.; Zuo, L. Design, Fabrication, Simulation and Testing of an Ocean Wave Energy Converter with Mechanical Motion Rectifier. *Ocean Eng.* **2017**, *136*, 190–200. [\[CrossRef\]](#)
10. Bowen, L.V. Design and Potential Power Recovery of Two Types of Energy Harvesting Shock Absorbers. *Energies* **2019**, *12*, 4710. [\[CrossRef\]](#)
11. Guan, D.; Cong, X.; Li, J.; Wang, P.; Yang, Z.; Jing, X. Theoretical Modeling and Optimal Matching on the Damping Property of Mechatronic Shock Absorber with Low Speed and Heavy Load Capacity. *J. Sound Vib.* **2022**, *535*, 117113. [\[CrossRef\]](#)
12. Vasic, D.; Chen, Y.Y.; Costa, F. Self-Powered Piezoelectric Energy Harvester for Bicycle. *J. Mech. Sci. Technol.* **2014**, *28*, 2501–2510. [\[CrossRef\]](#)
13. Abdelkareem, M.A.A.; Xu, L.; Ali, M.K.A.; Elagouz, A.; Mi, J.; Guo, S.; Liu, Y.; Zuo, L. Vibration Energy Harvesting in Automotive Suspension System: A Detailed Review. *Appl. Energy* **2018**, *229*, 672–699. [\[CrossRef\]](#)
14. Bowen, L.; Vinolas, J.; Olazagoitia, J.L.; Echavarri Otero, J. An Innovative Energy Harvesting Shock Absorber System Using Cable Transmission. *IEEE/ASME Trans. Mechatron.* **2019**, *24*, 689–699. [\[CrossRef\]](#)
15. Molina Arias, L.; Iwaniec, J.; Iwaniec, M. Modeling and Analysis of the Power Conditioning Circuit for an Electromagnetic Human Walking-Induced Energy Harvester. *Energies* **2021**, *14*, 3367. [\[CrossRef\]](#)
16. Hong, Y.; Temiz, I.; Pan, J.; Eriksson, M.; Boström, C. Damping Studies on Pmlg-Based Wave Energy Converter under Oceanic Wave Climates. *Energies* **2021**, *14*, 920. [\[CrossRef\]](#)
17. Jintanawan, T.; Phanomchoeng, G.; Suwankawin, S.; Kreepoke, P.; Chetchatree, P.; U-Viengchai, C. Design of Kinetic-Energy Harvesting Floors. *Energies* **2020**, *13*, 5419. [\[CrossRef\]](#)
18. Wu, X.; Qi, L.; Zhang, T.; Zhang, Z.; Yuan, Y.; Liu, Y. A Novel Kinetic Energy Harvester Using Vibration Rectification Mechanism for Self-Powered Applications in Railway. *Energy Convers. Manag.* **2021**, *228*, 113720. [\[CrossRef\]](#)

19. Zhang, Z.; Zhang, X.; Chen, W.; Rasim, Y.; Salman, W.; Pan, H.; Yuan, Y.; Wang, C. A High-Efficiency Energy Regenerative Shock Absorber Using Supercapacitors for Renewable Energy Applications in Range Extended Electric Vehicle. *Appl. Energy* **2016**, *178*, 177–188. [[CrossRef](#)]
20. Li, Z.; Zuo, L.; Kuang, J.; Luhurs, G. Energy-Harvesting Shock Absorber with a Mechanical Motion Rectifier. *Smart Mater. Struct.* **2013**, *22*, 025008. [[CrossRef](#)]
21. Li, Z.; Zuo, L.; Luhurs, G.; Lin, L.; Qin, Y.X. Electromagnetic Energy-Harvesting Shock Absorbers: Design, Modeling, and Road Tests. *IEEE Trans. Veh. Technol.* **2013**, *62*, 1065–1074. [[CrossRef](#)]
22. Guo, S.; Liu, Y.; Xu, L.; Guo, X.; Zuo, L. Performance Evaluation and Parameter Sensitivity of Energy-Harvesting Shock Absorbers on Different Vehicles. *Veh. Syst. Dyn.* **2016**, *54*, 918–942. [[CrossRef](#)]
23. Xie, L.; Cai, S.; Huang, G.; Huang, L.; Li, J.; Li, X. On Energy Harvesting from a Vehicle Damper. *IEEE/ASME Trans. Mechatron.* **2020**, *25*, 108–117. [[CrossRef](#)]
24. Xie, L.; Li, J.; Li, X.; Huang, L.; Cai, S. Damping-Tunable Energy-Harvesting Vehicle Damper with Multiple Controlled Generators: Design, Modeling and Experiments. *Mech. Syst. Signal Process.* **2018**, *99*, 859–872. [[CrossRef](#)]
25. Zhu, H.; Li, Y.; Shen, W.; Zhu, S. Mechanical and Energy-Harvesting Model for Electromagnetic Inertial Mass Dampers. *Mech. Syst. Signal Process.* **2019**, *120*, 203–220. [[CrossRef](#)]
26. Liu, Y.; Xu, L.; Zuo, L. Design, Modeling, Lab, and Field Tests of a Mechanical-Motion-Rectifier-Based Energy Harvester Using a Ball-Screw Mechanism. *IEEE/ASME Trans. Mechatron.* **2017**, *22*, 1933–1943. [[CrossRef](#)]
27. Li, X.; Liang, C.; Chen, C.A.; Xiong, Q.; Parker, R.G.; Zuo, L. Optimum Power Analysis of a Self-Reactive Wave Energy Point Absorber with Mechanically-Driven Power Take-Offs. *Energy* **2020**, *195*, 116927. [[CrossRef](#)]
28. Lin, T.; Wang, J.J.; Zuo, L. Efficient Electromagnetic Energy Harvester for Railroad Transportation. *Mechatronics* **2018**, *53*, 277–286. [[CrossRef](#)]
29. Yuan, Y.; Liu, M.; Tai, W.C.; Zuo, L. Design and Treadmill Test of a Broadband Energy Harvesting Backpack with a Mechanical Motion Rectifier. *J. Mech. Des. Trans. ASME* **2018**, *140*, 1–8. [[CrossRef](#)]
30. Yang, Y.; Pian, Y.; Liu, Q. Design of Energy Harvester Using Rotating Motion Rectifier and Its Application on Bicycle. *Energy* **2019**, *179*, 222–231. [[CrossRef](#)]
31. Wang, Z.; Zhang, T.; Zhang, Z.; Yuan, Y.; Liu, Y. A High-Efficiency Regenerative Shock Absorber Considering Twin Ball Screws Transmissions for Application in Range-Extended Electric Vehicles. *Energy Built Environ.* **2020**, *1*, 36–49. [[CrossRef](#)]
32. Li, H.; Zheng, P.; Zhang, T.; Zou, Y.; Pan, Y.; Zhang, Z.; Azam, A. A High-Efficiency Energy Regenerative Shock Absorber for Powering Auxiliary Devices of New Energy Driverless Buses. *Appl. Energy* **2021**, *295*, 117020. [[CrossRef](#)]
33. Salman, W.; Qi, L.; Zhu, X.; Pan, H.; Zhang, X.; Bano, S.; Zhang, Z.; Yuan, Y. A High-Efficiency Energy Regenerative Shock Absorber Using Helical Gears for Powering Low-Wattage Electrical Device of Electric Vehicles. *Energy* **2018**, *159*, 361–372. [[CrossRef](#)]
34. Li, X.; Martin, D.; Liang, C.; Chen, C.A.; Parker, R.G.; Zuo, L. Characterization and Verification of a Two-Body Wave Energy Converter with a Novel Power Take-off. *Renew. Energy* **2021**, *163*, 910–920. [[CrossRef](#)]
35. Costanzo, L.; Lin, T.; Lin, W.; Schiavo, A.L.; Vitelli, M.; Zuo, L. Power Electronic Interface with an Adaptive MPPT Technique for Train Suspension Energy Harvesters. *IEEE Trans. Ind. Electron.* **2020**, *68*, 8219–8230. [[CrossRef](#)]
36. Guo, S.; Xu, L.; Liu, Y.; Guo, X.; Zuo, L. Modeling and Experiments of a Hydraulic Electromagnetic Energy-Harvesting Shock Absorber. *IEEE/ASME Trans. Mechatron.* **2017**, *22*, 2684–2694. [[CrossRef](#)]